

Laser-induced cavitation based micropump†

Rory Dijkink^a and Claus-Dieter Ohl^{a,b}

Received 23rd April 2008, Accepted 26th June 2008

First published as an Advance Article on the web 28th August 2008

DOI: 10.1039/b806912c

Lab-on-a-chip devices are in strong demand as versatile and robust pumping techniques. Here, we present a cavitation based technique, which is able to pump a volume of 4000 μm^3 within 75 μs against an estimated pressure head of 3 bar. The single cavitation event is created by focusing a laser pulse in a conventional PDMS microfluidic chip close to the channel opening. High-speed photography at 1 million frames s^{-1} resolves the flow in the supply channel, pump channel, and close to the cavity. The elasticity of the material affects the overall fluid flow. Continuous pumping at repetition rates of up to 5 Hz through 6 mm long square channels of 20 μm width is shown. A parameter study reveals the key-parameters for operation: the distance between the laser focus and the channel, the maximum bubble size, and the chamber geometry.

Introduction

Bubbles are widely used as actuators in microfluidic devices. The most well known application is that in ink-jet printers.¹ There the explosive-like growth of vapor bubbles accelerates liquid through a nozzle and finally into a droplet for its deposition onto paper. These explosively expanding and shrinking bubbles which are commonly termed cavitation bubbles have recently received increasing attention for microfluidic applications. Cavitation enhances microfluidic mixing,² allows for cell manipulation such as cell surgery³ or cell lyses,⁴ and can be used for drug delivery within the micro-vascular system of a human body.⁵

In contrast, cavitation is occurring in some flow configurations where it is undesirable. Here, research focuses on the prevention of cavitation in microfluidics, for example in microfluidic phase-change heat-exchangers.⁶

Yet, in the authors view, the advantages cavitation phenomena offer for microfluidic applications greatly surpass their disadvantages. Because of the rapid expansion and the flow focusing ability^{7,8} the liquid is accelerated to very high speeds. Thus, the prevalent low Reynolds number regime is overcome. This property was utilized in a recent study in Venugopalan's group for the rapid mixing of chemicals in lab-on-a-chip devices,² an application which is very difficult to achieve by other means.⁹ A second application where cavitation is utilized is pumping. Here a high Reynolds number allows for flow asymmetry, such that

the forward and back-stroke of the device possess different flow patterns. Tsai and Lin developed a bubble actuated micropump based on the difference in flow resistances of nozzles on the flow direction¹⁰ where an oscillating bubble creates aperiodic flow which is given a preferred flow direction through the chip geometry. A very similar concept was utilized by Yin & Prosperetti where a vapor bubble is created at some distance from the center of a long channel, leading to a flow towards the longer half of the channel.^{11,12} Another concept of cavitation based pumps utilizes a special flow phenomenon when the bubble collapse progresses close to a rigid boundary. There, the bubble oscillation is strongly affected: during the shrinkage of the bubble the distant bubble interface bulges inwards and develops into a re-entrant jet directed towards the rigid boundary. Now, the trick in a pumping configuration is that the boundary has a small opening at the position where the jet would impact and it is small enough that the jetting phenomena is still occurring.¹³ The hole permits the transport of liquid from above the boundary. Without this jetting phenomenon there would be flow through the boundary, however, the volume flux during bubble expansion and shrinkage would balance.

In this work we will scale the jetting flow concept down to lab-on-a-chip systems. In contrast to prior attempts of electrode or heater generated bubbles, we will make use of laser generated bubbles.⁸ The advantages of using an optical method is that a simple soft lithography technique can be used, no connections and wiring of the device is needed, and pumping can be achieved at many places on the chip. Additionally, the bubbles are transient vapor bubbles which quickly condense after actuation. Thus the pumping is not affected by any gas diffusion or creation of residual gas bubbles.

We will first explain the experimental setup to generate cavitation in lab-on-a-chip systems and how to study the pumping effect. Then the liquid motion during and after the pumping stroke is analyzed which reveals an important characteristic of elastic material based microfluidic devices. The experimental

^aPhysics of Fluids, Faculty of Science and Technology, University of Twente, PO Box 217, 7500, AE, Enschede, The Netherlands. E-mail: R.J.Dijkink@utwente.nl; Fax: +31 53489 8068; Tel: +31 53489 2470

^bDivision of Physics and Applied Physics, School of Physical and Mathematical Sciences, Nanyang Technological University, 637371, Singapore. E-mail: CDOhl@ntu.edu.sg; Fax: +65 6794 1325; Tel: +65 6513 8039

† Electronic supplementary information (ESI) available: Micro-system fabrication and movie of the jetting phenomenon. See DOI: 10.1039/b806912c

analysis is concluded with a parameter study of the bubble positioning/size and the chamber geometry.

Materials and methods

Microfluidic system and experimental setup

The microfluidic devices are made of PDMS (polydimethylsiloxane) with standard soft lithography techniques (see microsystem fabrication in ESI†). The microfluidic device is bonded to a coverslip and viewed through an inverted microscope (CF 40, Carl Zeiss GmbH, Göttingen, Germany) with the coverslip facing down. The liquid is injected through tubing connected to the reservoirs, see Fig. 1. The long thin channels have a square cross section of $20 \times 20 \mu\text{m}^2$. The channel is passing through a chamber; the distance of the upper reservoir to the chamber inlet is 0.6 mm and 6 mm to the lower reservoir. Two different geometries are used, a square chamber with $200 \times 200 \mu\text{m}^2$, and a chamber with a flat boundary connected to the upper channel and a semicircular boundary connected to the lower one, see Fig. 1a. The slabs of PDMS are about 4 mm thick.

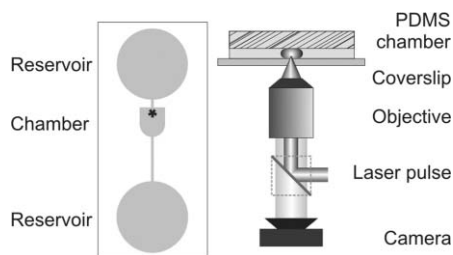


Fig. 1 (a) Design of the microfluidic system (not to scale) to study the pumping effect: it consists of two circular fluid reservoirs connected *via* thin channels with the pumping chamber. The upper channel is 0.6 mm and the lower channel 6 mm long. The black asterisk denotes a typical location for the laser focus. (b) Sketch of the optical path for the generation of the cavitation bubble and the high-speed recording. The PDMS chip is bonded on top of a glass coverslip.

Cavitation generation

Single 6 ns long light pulses from a frequency doubled Q-switched Nd:YAG laser (NewWave, Solo PIV, wavelength 532 nm) are focused in the microfluidic chamber with a $10\times$ microscope objective (NA 0.25). The liquid is dyed with an aqueous solution of Direct Red 81 (DR81, Sigma-Aldrich Chemie, Zwijndrecht, Netherlands) resulting in a light absorption coefficient of 20.000 m^{-1} to 50.000 m^{-1} at the laser wavelength. The range of the laser energy is between 10 μJ and 50 μJ .

High-speed recording

The scene is recorded with a high-speed camera (HPV-1, Shimadzu, Duesseldorf, Germany). The laser and optical path of the camera are separated with suitable filters and a dichroic mirror. An intense fiber optic light (HL-1, Olympus, Zoeterwoude, The Netherlands) is necessary to obtain sufficient contrast to observe not only the bubble but also the tracer particles at the maximum frame rate of 1 million frames per second.⁸

Flow-visualization with particle image velocimetry

Using a standard particle image velocimetry (PIV) algorithm¹⁴ which correlates successive images from the high-speed recording, local flow velocities are obtained. For the algorithm an interrogation window of 8×8 pixels is used at a spacing of half the interrogation window size. The polystyrene tracer particles have a diameter of $2 \mu\text{m}$ (Duke Scientific, Fremont, CA, USA). In contrast with conventional PIV experiments using a light sheet technique to constrain the image plane, here a relatively low NA objective records the particles within the chamber not only in a thin focal plane image plane but over the entire cross section. Therefore, the magnitude of the velocities is only a lower estimate of the chamber's center velocity.

Additionally to the PIV algorithm applied inside the chamber, the particle displacement within the channels are measured manually.

We assume that the particles can follow the flow field with little slip. This is justified by the good agreement of the theoretical flow field with the measured one in our previous work using the same type of particles.⁸

Continuous pumping

For the continuous pumping experiments the microfluidic system was submerged in a water filled glass cuvet which was then placed on top of the microscope. For the recording of the fluid motion a sensitive double-frame camera (Sensicam-QE, PCO, Kehlheim, Germany) is used in combination with a strobed high intensity LED (V-Star, Lumiled, Philips).

Image and motion analysis is done with Matlab and the image processing toolbox (Mathworks, Natick, MA, USA).

Results and discussion

Bubble dynamics and flow field inside the chamber

A single pump stroke consists of the rapid bubble expansion-collapse cycle followed by a slower residual flow. The bubble oscillations occur typically within 10 μs , the residual flow dies out only after about 80 μs . We discuss first the bubble expansion-collapse cycle together with the flow pattern.

The high speed recordings allow visualizing both the bubble shape and the flow pattern as shown in Fig. 2 and movie in ESI.† Here, several frames from a 1 million frames s^{-1} recording depict the liquid slightly darker than the surrounding PDMS. The liquid is seeded with $2 \mu\text{m}$ sized particles making the channel and pumping chamber easily distinguishable. The first image of Fig. 2 depicts the device just before the laser-induced cavitation bubble is generated. The second image displays the bubble initiation and shows the rapidly expanding bubble growing on the top wall of the chamber at the channel entrance with part of the bubble extending into the channel.

The rapid/explosive growth of the bubble and the limited exposure time of 500 ns leads to a blurred bubble shape; yet we can estimate a lower radial velocity of the bubble during the first microsecond of at least 40 m s^{-1} ! Due to the motion blurring the PIV algorithm isn't able to track the velocity close to the bubble interface, yet we see a nicely resolved outwards pointing flow

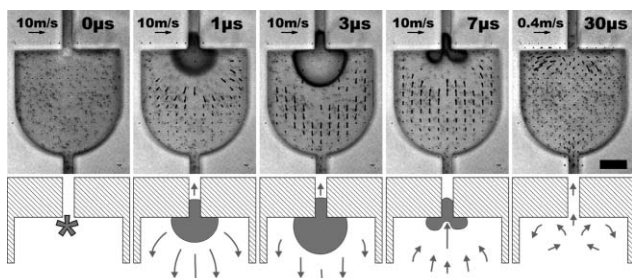


Fig. 2 Selected high speed movie frames showing different stages of the bubble growth and collapse. The images include experimentally obtained velocity vector fields with a schematic representation of the flow field below each frame. The first image shows the chamber just before bubble initiation, then $1 \mu\text{s}$ later the bubble is rapidly expanding, reaching its maximum size in the third image ($t = 3 \mu\text{s}$). Afterwards the bubble starts to collapse creating a jet which is directed into the channel as can be seen in the fourth image. In the last image the bubble has completely disappeared leaving some circulating flow behind. Please note that the scale of the vectors, denoted by the reference arrow in the upper left corner of each frame, in the first 4 images is 25 times larger than the residual flow shown after the bubble has disappeared (5th frame). The black bar in the lower right corner of the last frame denotes $50 \mu\text{m}$.

pattern further away which drops almost to zero at the opposing channel entrance.

Because the lateral size of the bubble is much larger than the height of the chamber, the bubble obtains a pancake shape. In the third frame of Fig. 2, the bubble has gained its maximum expansion with some part of the volume extending into the channel. Thereafter, the far field pressure drives the bubble to shrink. During the accelerated shrinkage/collapse of the bubble a jetting flow develops towards the upper channel resembling the collapse in semi-infinite liquid,^{15,16} $t = 3 \mu\text{s}$ in Fig. 2. The quasi two-dimensional nature of this experiment allows a detailed look on the jet shape. The jet accelerates through the bubble and is aimed towards the nearby boundary but because of the channel the jet doesn't impact on a PDMS chamber wall but flows into the channel. As we will show in the later discussions, it is this jetting which is important for the pumping effect.

In the later course of the bubble oscillation the bubble splits into two parts, $t = 7 \mu\text{s}$ and it disappears. The flow pattern shown in frame $t = 30 \mu\text{s}$ is a time average from $t = 10 \mu\text{s}$ to $t = 30 \mu\text{s}$. Upon careful inspection two counter rotating vortices remain, left and right of the upper channel entrance. The velocity after the bubble collapse is much lower; we find velocities of up to 0.4 m s^{-1} which quickly drop further from the upper channel inlet.

Flow inside the channel

Next we study the flow inside the channel and correlate it with the bubble dynamics. Here, we make use of individual tracked particles to quantify the fluid motion. Clearly, a boundary layer in the channel will lead to an uneven velocity distribution across the channel. Therefore, multiple particles are tracked; in general particles closer to the channel's center experience a larger displacement. Fig. 3 depicts the displacement of several particles in the upper (solid black lines) and lower channel (dashed grey) in combination with the bubble dynamics. For clarity, we have selected an experiment with a moderately large pumping effect.

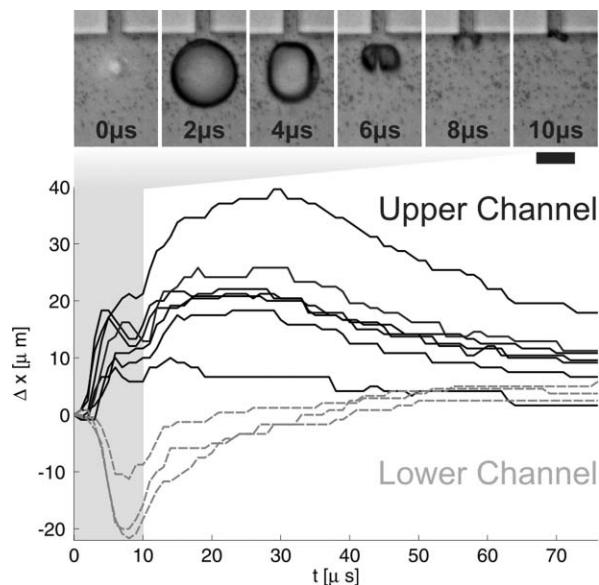


Fig. 3 Another cavitating bubble is shown, this time located a little further from the channel opening. To estimate the induced flow speeds inside the channel, separate particles were tracked and plotted against time in the graph below the movie frames. The solid black lines are particles traveling in the pumping channel of which the opening can be seen in the images, for continuity some particles in the lower feed channel were also tracked and are displayed by the dashed grey lines. The light grey area between $0\text{--}10 \mu\text{s}$ denotes where the movie frames are situated on the graphs timeline. The black bar below the last frame denotes $50 \mu\text{m}$.

We will first concentrate on the particle motion in the upper channel.

The bubble dynamics lasts again for $10 \mu\text{s}$ and selected frames are depicted on top of the graph in Fig. 3. The bubble expands further from the boundary as compared to Fig. 2, yet during jetting, the bubble moves close to the boundary ($t = 8 \mu\text{s}$). This motion of the bubble centroid towards the boundary is well known in studies of cavitation bubbles close to semi-infinite boundaries.^{17,18}

The tracer particle motion reveals the rapid motion during and following the bubble dynamics. When the bubble expands, $t < 4 \mu\text{s}$ particles in the upper channel are accelerated upwards, whereas particles in the lower channel move downwards. This motion can be solely explained by the radial expansion of the bubble. In contrast, when the bubble starts to shrink, most of the upper particles are "sucked" towards the chamber, *i.e.* if both fluid motions would be symmetric no fluid displacement would remain. Yet, we find a lesser back flow, *e.g.* the second largest upward displacement graph moves approx. $18 \mu\text{m}$ forward but only $5 \mu\text{m}$ backward. Most likely this is caused by the translational motion of the bubble centroid towards the upper channel: it is a superposition of the radial inflow and the translational, dipolar flow. During expansion however, the added mass¹⁸ of the bubble prevents a large movement of the bubble centroid from the wall. Another observation is that the particle motion lags a few microseconds behind the bubble oscillations, *e.g.* maximum displacement during the expansion is observed between $t = 5 \mu\text{s}$ to $t = 7 \mu\text{s}$, whereas the bubble reaches maximum size at $t = 4 \mu\text{s}$.

After the bubble expansion we find again a jet flow through the bubble which splits it into two parts at around $t = 9 \mu\text{s}$ and reaches the upper channel inlet. Interestingly, it is at this time that all particles in the upper channel change direction. The particle motion prevails for $20 \mu\text{s}$, long after the bubble has vanished. We explain this upward directed flow as a result of the continuing jet flow which lasts long after the bubble has disappeared. An equally valid description of the flow is that of two counter-rotating vortices left and right of the channel inlet accelerating liquid upwards at their contact line.

Effect of PDMS compliance

The solid lines in Fig. 3 exhibit a flow reversal in the upper channel at times $t > 30 \mu\text{s}$ reducing the net displacement of the particles to about 40%–50% of their maximum upwards travel.

To investigate the cause of this flow reversal we studied the flow into the chamber by tracking particles in the lower feeding channel. Their trajectories are plotted in the same graph, Fig. 3 with dashed lines. During bubble expansion and early collapse, $t \leq 8 \mu\text{s}$, the particles move away from the chamber. The maximum displacement is in the range from $10 \mu\text{m}$ to $20 \mu\text{m}$ and of the same magnitude as in the upper channel during bubble activity. Interestingly, no back flow occurs during the collapse of the bubble. Simple mass conservation in rigid structures would demand that the sum of the displaced volumes in the upper and lower channel is equal to the bubble volume and again zero after the bubble has disappeared. We now study the apparent missing volume by plotting the averaged volumes of the bubble, V_b , and the displaced upper and lower channel volume, $V_{uc} + V_{lc}$, in Fig. 4. The volumes V_{uc} and V_{lc} are calculated from the average of the displacement, Fig. 3, and the known channel cross section with volume leaving the chamber taken positive. The bubble volume is extracted by image processing assuming a generalized cylindrical bubble shape. The dashed-dotted line shows that the bubble obtains approximately a volume of $1.5 \times 10^5 \mu\text{m}^3$ which

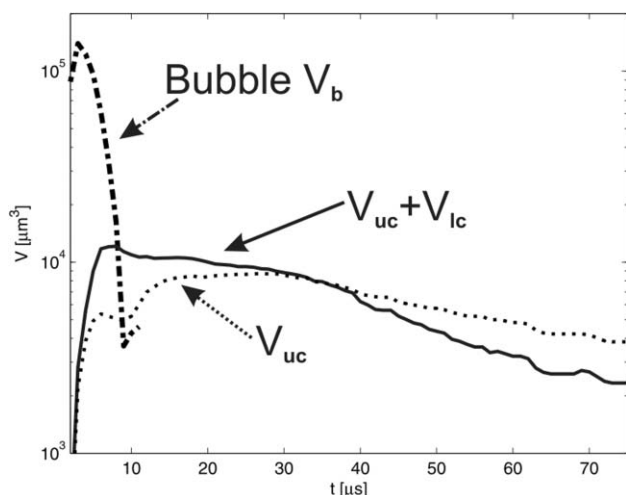


Fig. 4 Volume balance during the pumping stroke: the void or bubble volume (dashed-dotted line), V_b , is compared with the total displaced liquid volume $V_{uc} + V_{lc}$ on a logarithmic scale. The difference between $V_{uc} + V_{lc}$ and V_b can be explained by a deformation of the pumping chamber. After the bubble has disappeared the total displaced volume is slowly relaxing to zero.

isn't balanced by the displaced channel volume of $1.3 \times 10^4 \mu\text{m}^3$. This discrepancy can be explained by a deformation of the fluid chamber. For the maximum bubble size we estimate that an expansion of the chamber of $1.7 \mu\text{m}$ towards the PDMS cover and the glass plate would already account for the missing volume. During the bubble shrinkage the situation reverses; the displaced volume, $V_{uc} + V_{lc}$, is larger than the bubble volume for $t > 7 \mu\text{s}$. This means that the chamber has shrunk.

After the bubble has disappeared, $t = 12 \mu\text{s}$, we observe a steady decline of $V_{uc} + V_{lc}$ with time. This is presumably caused by the expansion of the chamber back to its original size, sucking liquid back into the chamber. At time $t = 35 \mu\text{s}$, V_{lc} becomes negative, thus both the upper and the lower channels now have a displaced volume in the same upwards direction. At the end of the pumping stroke, V_{uc} and V_{lc} become equal in magnitude but with opposing signs, *i.e.* the two volume displacements will be in the same direction and $V_{uc} + V_{lc}$ is zero. For a net volume displacement over a pumping stroke $|V_{uc}| > 0$ is required with the sign depending on the pumping direction.

Continuous pumping

Fig. 4 shows a steady decline of the displaced volume V_{uc} reaching $4 \times 10^3 \mu\text{m}^3$ after $75 \mu\text{s}$. This is equivalent with the averaged displacement of $10 \mu\text{m}$ as shown in Fig. 3 (solid lines). One could argue that for longer times the net displacement and thus the pumping effect might be canceled.

To prove that this is not the case but a considerable net displacement remains the particles positions long after the bubble oscillation have been recorded. Additionally, the laser creating the bubble is operated in a continuous pulsing mode. Fig. 5 shows the particle displacement for 1 Hz laser frequency every second laser pulse and 2 ms after the pumping stroke. Two particles are marked with a circle. The upper one moves approximately $10 \mu\text{m}$ every two laser pulses. The lower particle which is imaged out of focus translates after some transition period (1st–9th pump stroke) with the same displacement. This demonstrates that the remaining net displacement is indeed existent and $5 \mu\text{m}$ per stroke, about half the displacement which we find after $75 \mu\text{s}$, see Fig. 4.

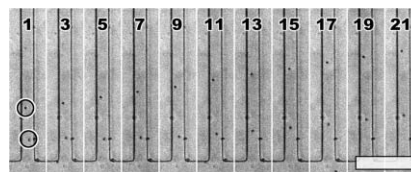


Fig. 5 Pumping motion where the laser is run at 1 Hz for multiple strokes: an image was taken 2 ms after every pumping stroke, which is indicated at the top of each frame. Two tracer particles are encircled in the first frame with the top particle showing an average displacement of approximately $5 \mu\text{m}$ per cycle or $10 \mu\text{m}$ between frames. The white bar in the lower right corner denotes $100 \mu\text{m}$.

Additionally, Fig. 5 shows that a continuous operation of the pump is possible. The maximum frequency of the laser used so far was 5 Hz for 500 consecutive pulses. Under this operation condition, stable pumping was found without the formation of residual gas bubbles (see sets 5 and 6 in Table 1, discussion below). The repetition rate was limited by the experimental setup

Table 1 Summary of the final liquid displacements achieved per stroke for bubbles with different sizes R_{\max} and relative distances to the nearest channel opening h/R_{\max} . Here a square chamber is connected to again a longer downwards channel and a shorter upwards channel. The number of particles tracked in each set is denoted by n

#	$R_{\max}/\mu\text{m}$	h/R_{\max}	Square chamber length/ μm	Pump direction	n	Stroke freq./Hz	$[\Delta x/\text{stroke}]/\mu\text{m}$
1	42 ± 1	0.69 ± 0.05	200	Down	8	1	2.3 ± 0.4
2	41 ± 1	0.52 ± 0.05	200	Up	8	1	2.5 ± 0.3
3	52 ± 1	0.69 ± 0.05	200	Down	8	1	4.9 ± 1.1
4	50 ± 1	0.64 ± 0.05	200	Up	9	1	3.9 ± 0.7
5	47 ± 1	0.59 ± 0.06	200	Down	7	5	5.4 ± 3.3
6	43 ± 1	0.57 ± 0.05	200	Up	9	5	4.1 ± 0.6

and not by the pump itself. The maximum pumping rate has not been explored. In the current design we expect that an upper boundary is most likely imposed by the heating of the PDMS and the liquid from the laser pulses causing an out-gassing of the liquid. Depending on the size and location residual gas bubbles might temporarily block the supply channels.

Parameter study

After reporting on the details of the pumping stroke we now change the easily accessible experimental parameters of the bubble pump, namely bubble size (R_{\max}), distance from the upper channel entrance (h), and to some extent also the chamber geometry. For this study, separate bubbles are created at different locations on the center line of the channel starting at the straight upper wall ($h = 0 \mu\text{m}$) and ending at the lower semicircular wall ($h = 200 \mu\text{m}$). On the y-axis of Fig. 6 we plot the maximum displacement of the tracer particles in the supply channels. For distances $h < 100 \mu\text{m}$ the displacement of particles in the upper channel is plotted whereas for $h > 100 \mu\text{m}$ the particles in the lower channel are studied. Additionally, the laser energy is varied, which leads to three data sets with maximum radii

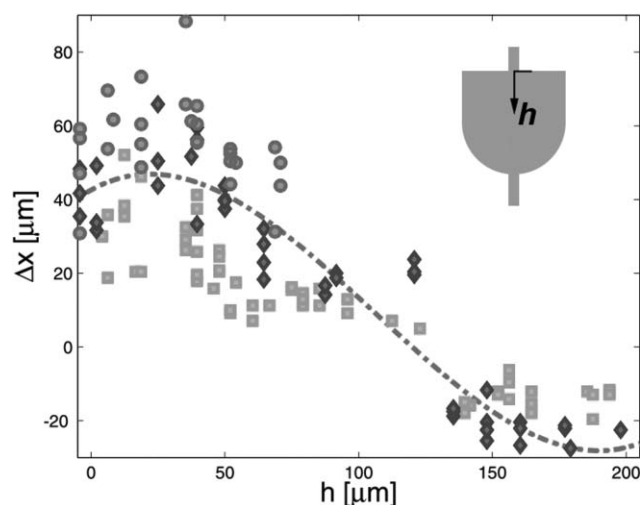


Fig. 6 The maximum particle displacements (Δx) are plotted *versus* the position of the bubble generation, h , starting with 0 at the top channel, see sketch. The distance h is increased from $-5 \mu\text{m}$ to the lower supply channel at $h = 200 \mu\text{m}$. Half way through the chamber, $h = 100 \mu\text{m}$, the pump switches direction and the maximum displacement of the particles in the lower channel are plotted. These measurements were done for three different bubble sizes ($R_{\max} = 37 \mu\text{m}$ \square , $44 \mu\text{m}$ \diamond , and $50 \mu\text{m}$ \circ). The dashed-dotted line is a third-order polynomial fit to the displacement from bubbles of $R_{\max} = 44 \mu\text{m}$.

of $R_{\max} = 37.5 \mu\text{m}$, $43.8 \mu\text{m}$, and $50.0 \mu\text{m}$ plotted as squares, diamonds, and circles, respectively. Although we don't know the energy absorbed in the liquid, the energy setting of the laser was increased by 50% and 100% to increase the bubble size for the latter two, respectively.

Let us first discuss the medium sized bubbles (diamonds in Fig. 6). Although there is some scatter in the data, we find two clear extremes for the maximum displacement, namely at $25 \mu\text{m}$ and $170 \mu\text{m}$. Thus optimum pumping is observed when the bubble is created at about $30 \mu\text{m}$ or about 80% of maximum bubble radius from the respective channel openings. The larger and smaller bubbles—circles and square, respectively—seem to support this 80% value.

Another interesting observation is that the maximum displacement for $h > 100 \mu\text{m}$ (in the lower channel) is smaller than for $h < 100 \mu\text{m}$ (in the upper channel); a larger displacement is found for the flat boundary. This can be explained with a rounded boundary hindering the inflow from the sides more as compared to a flat boundary.

Another asymmetry of the system is the different channel lengths, see Fig. 1. Indeed an asymmetry in the channel lengths was exploited in the “blinking bubble” pump.¹¹ There however, the pumping was towards the channel with the higher resistance, which is opposite to our configuration; pumping occurs into the shorter channel. For our geometry we don't expect that this channel length difference affects the liquid displacement, which is also supported by the data presented in Table 1. In general larger bubbles show larger displacements per stroke independent of the direction of the pumping. Interestingly, the displacement at high stroke frequency increases (see sets 5 and 6 in Table 1); possibly some residual flow is generated or the liquid is heated up thus decreasing its viscosity. Clearly further experiments are needed to evaluate the limits of continuous pumping.

Comparison with unconstrained jetting pump

The bubble operated pump presented in this work is very much related to the jetting bubble pump invented by Khoo and Klaseboer (theory in ref. 19 and experiment in ref. 13). In fact, the motivation of this work is to demonstrate that the jet based pumping mechanism works also in a lab-on-a-chip device. Yet, there are distinct differences in design and fluid dynamics. First, the pump of Khoo and Klaseboer operates in an infinite or very large container with millimetres sized bubbles, whereas here, the bubble is in the range of tens of micrometres and the bubble is constrained by an elastic material (PDMS). Our experimental data suggest that the chamber expands during the explosive

growth and indents during bubble collapse. Thus, only some amount of the fluid displaced by the bubble is pumped into the channels; we estimated in the experiment shown in Fig. 4 about 10%.

After the bubble has disappeared the flow into the channel continues and increases to a maximum displacement after which it decreases again; this extremum has not been observed in Khoo's and Klaseboer's experiments,¹³ they did not find a flow reversal which is very evident in our experiments.

This back flow may be explained with the second difference between both experimental realizations: in the present work the pumping chamber is connected to long and thin supply channels, whereas a very short and thick connecting channel was used in the previous work. Thin channels, however, can be responsible for a significant viscous pressure head. Let's estimate a lower bound of this pressure head assuming cylindrical geometry and a developed flow, *i.e.* a Poiseuille flow. Thus, the pressure gradient dP/dx is given by

$$\frac{dP}{dx} = 4\mu u_{\max} R^{-2}, \quad (1)$$

where μ is the dynamic viscosity $10^{-3} \text{ kg m}^{-1} \text{ s}^{-1}$, u_{\max} the center velocity, and $R \approx 10 \text{ }\mu\text{m}$ the channel diameter. A value for the center velocity is obtained from the maximum displacement, see Fig. 3, at time $t = 30 \text{ }\mu\text{s}$ giving $u_{\max} \approx 1.3 \text{ m s}^{-1}$ and leading to a viscous pressure gradient of approx. $5.2 \times 10^7 \text{ Pa m}^{-1}$. For a total channel length of 6.6 mm we obtain a considerable pressure head of about 3.4 bar. This value is only a lower bound, as the flow field is not developed leading to larger velocity gradients at the channel boundaries.

We speculate that this pressure head leads to the observed quick stop of the flow and to the following flow reversal. Nevertheless, a net displacement and thus a pumping effect was observed which proves the applicability of cavitation based pumps in elastic microfluidic devices operating even against high viscous pressure heads of a few bars.

The advantage of using a laser to generate cavitation is that no additional manufacturing step in the PDMS chip fabrication is necessary, no mechanical or electrical connections are needed for operation, and already existing designs may be utilized. For operation the laser has to be focused on the wider side of a channel constriction. The main requirements are an optical transparent lab-on-a-chip and a means for conversion of the pulsed laser energy into a vapor bubble. This can be achieved either as presented here by using a laser-light absorbing dye or as demonstrated by Venugopalan's group² by multiphoton ionization of the liquid. The phenomenon is based on high Reynolds number flows. Thus for more viscous liquids, adjustments to the geometry of the channel and/or size of the bubble are needed to allow for a cavitation based pump.

Conclusions

In conclusion we have demonstrated that single cavitation bubbles in microfluidics allows for the repeatable and precise control of picolitre volumes. The pumping effect utilizes a jetting phenomenon which has been studied and characterized with high-speed imaging.

For the inspected parameters optimum pumping was found when the distance between the laser focus and the channel inlet is about 80% of the maximum bubble radius. Additionally, continuous pumping has been demonstrated: for the maximum repetition rates tested which was 5 Hz we obtained repeatable operation without the formation of residual gas bubbles.

The technique presented in this article is already applicable for standard PDMS devices. We expect that further improvement in volume flux can be achieved with a modified channel layout. For example, Khoo's and Klaseboer's experiment¹³ demonstrates that higher volume fluxes can be achieved for wider channels. Also very likely some of the backflow can be eliminated by implementing diffuser type geometries along the channel, see ref. 10.

At last we want to mention, that by moving the laser beam to different locations, more complex pumping operations may be realized, for example, pumping liquids from one chamber into a set of branching channels. Here, the amount of pumped volume can be adjusted by the distance of the bubble to the channel or through the laser energy. The position of the laser focus may be selected by a switching mirror or through diffractive elements, for example spatial light modulators. Research to automate fluid handling with these techniques is currently underway in the author's labs.

Acknowledgements

For initial experiments on the pumping mechanism we greatly acknowledge the help of M. Kolen and M.J. van der Meulen. Financial support through VIDI N.W.O, The Netherlands and NTU Tier 1 RG39/07. Further we are thankful for the assistance in the microfabrication from S. Le Gac and J. Li.

Notes and references

- 1 H. P. Le, *J. Imaging Sci. Technol.*, 1998, **42**, 49–62.
- 2 A. N. Hellman, K. R. Rau, H. H. Yoon, S. Bae, J. F. Palmer, K. S. Philips, N. L. Allbritton and V. Venugopalan, *Anal. Chem.*, 2007, **79**, 4484–4492.
- 3 A. Vogel, J. Noack, G. Hüttman and G. Paltauf, *Appl. Phys. B: Lasers Opt.*, 2005, **81**, 1015–1047.
- 4 S. Le Gac, E. Zwaan, A. Van Den Berg and C. D. Ohl, *Lab Chip*, 2007, **7**, 1666–1672.
- 5 M. W. Miller, D. L. Miller and A. A. Brayman, *Ultrasound Med. Biol.*, 1996, **22**, 1131–1154.
- 6 C. Mishra and Y. Peles, *Phys. Fluids*, 2005, **17**, 113602.
- 7 B. W. Zeff, B. Kleber, J. Fineberg and D. Lathrop, *Nature*, 2000, **407**, 401–404.
- 8 E. Zwaan, S. Le Gac, K. Tsuji and C. D. Ohl, *Phys. Rev. Lett.*, 2007, **98**, 254501.
- 9 J. M. Ottino and S. Wiggins, *Philos. Trans. R. Soc. London, Ser. A*, 2004, **362**, 923–935.
- 10 H. Jr. Tsai and L. Lin, *J. Microelectromech. Syst.*, 2002, **11**, 665–671.
- 11 Z. Yin and A. Prosperetti, *J. Micromech. Microeng.*, 2005, **15**, 643–651.
- 12 Z. Yin and A. Prosperetti, *J. Micromech. Microeng.*, 2005, **15**, 1683–1691.
- 13 K. S. F. Lew, E. Klaseboer and B. C. Khoo, *Sens. Actuators, A*, 2007, **133**, 161–172.
- 14 We use the package URAPIV from <http://urapiv.wordpress.com/>.
- 15 W. Lauterborn and H. Bolle, *J. Fluid Mech.*, 1975, **72**, 391–399.
- 16 J. R. Blake and D. C. Gibson, *J. Fluid Mech.*, 1981, **111**, 123–140.
- 17 Y. Tomita and A. Shima, *Acustica*, 1990, **71**, 161–171.
- 18 T. B. Benjamin and A. T. Ellis, *Philos. Trans. R. Soc. London, Ser. A*, 1966, **260**, 221–240.
- 19 B. C. Khoo, E. Klaseboer and K. C. Hung, *Sens. Actuators, A*, 2005, **118**, 152–161.